

46. F. J. Hilgen and C. G. Langereis, *Terra Nova* **1**, 409 (1989).
47. K. Yemane, R. Bonnefille, H. Faure, *Nature* **318**, 653 (1985).
48. R. Bonnefille, A. Vincens, G. Buchet, *Palaeogeogr. Palaeoclimatol. Palaeoecol.* **60**, 249 (1987); G. WoldeGabriel *et al.*, *Nature* **371**, 330 (1994).
49. T. E. Cerling, *ibid.* **97**, 241 (1992).
50. S. Leroy and L. Dupont, *ibid.* **109**, 295 (1994).
51. R. Bonnefille, *Nature* **303**, 487 (1983).
52. E. S. Vrba, G. H. Denton, M. L. Prentice, *Ossa* **14**, 127 (1989).
53. H. B. Wesselman, *S. Afr. J. Sci.* **81**, 260 (1985).
54. C. K. Brain, *Annex Transv. Geol. Soc. S. Afr. J. Sci.* **84**, 1 (1981).
55. E. S. Vrba, in *Paleoclimate and Evolution with Emphasis on Human Origins*, E. Vrba, G. Denton, L. Burckle, T. Partridge, Eds. (Yale Univ. Press, New Haven, CT, in press).
56. F. E. Grine, *S. Afr. J. Sci.* **82**, 87 (1986).
57. R. G. Klein, in *Evolutionary History of the "Robust" Australopithecines*, F. E. Grine, Ed. (de Gruyter, New York, 1988).
58. C. S. Feibel, F. H. Brown, I. McDougall, *Am. J. Phys. Anthropol.* **78**, 595 (1989).
59. W. Kimbel, in (55).
60. F. Schrenk, T. G. Bromage, C. G. Betzler, U. Ring, Y. M. Juwayeyi, *Nature* **365**, 833 (1993); A. Hill, S. Ward, A. Dieno, G. Curtis, R. Drake, *ibid.* **355**, 719 (1992).
61. B. Wood, *ibid.* **355**, 783 (1992).
62. J. W. K. Harris, in *African Archaeological Review*, N. David, Ed. (Cambridge Univ. Press, Cambridge, 1983), p. 3.
63. C. C. Swisher III *et al.*, *Science* **263**, 1118 (1994).
64. B. Aslaw *et al.*, *Nature* **362**, 732 (1992).
65. J. D. Clark, in *Human Ecology in Savanna Environments*, D. R. Harris, Ed. (Academic Press, London, 1980), pp. 41–71.
66. Technical assistance was provided by A. Esmay, L. Baker, P. Malone, and M. Horowitz. Comments and criticisms on initial versions of this manuscript were provided by F. Brown, L. Burckle, W. Kimbel, A. McIntyre, W. Ruddiman, F. Sirocko, B. Wood, E. Vrba, and three anonymous reviewers. I thank N. Shackleton for providing his ODP Leg 138 oxygen isotopic data and R. Tiedemann for supplying his eolian record from site 659. This work was supported by the Ocean Sciences Division of NSF. This is Lamont-Doherty Earth Observatory contribution number 5386.

RESEARCH ARTICLE

Sulfite Reductase Structure at 1.6 Å: Evolution and Catalysis for Reduction of Inorganic Anions

Brian R. Crane, Lewis M. Siegel, Elizabeth D. Getzoff*

Fundamental chemical transformations for biogeochemical cycling of sulfur and nitrogen are catalyzed by sulfite and nitrite reductases. The crystallographic structure of *Escherichia coli* sulfite reductase hemoprotein (SiRHP), which catalyzes the concerted six-electron reductions of sulfite to sulfide and nitrite to ammonia, was solved with multiwavelength anomalous diffraction (MAD) of the native siroheme and Fe₄S₄ cluster cofactors, multiple isomorphous replacement, and selenomethionine sequence markers. Twofold symmetry within the 64-kilodalton polypeptide generates a distinctive three-domain α/β fold that controls cofactor assembly and reactivity. Homology regions conserved between the symmetry-related halves of SiRHP and among other sulfite and nitrite reductases revealed key residues for stability and function, and identified a sulfite or nitrite reductase repeat (SNiRR) common to a redox-enzyme superfamily. The saddle-shaped siroheme shares a cysteine thiolate ligand with the Fe₄S₄ cluster and ligates an unexpected phosphate anion. In the substrate complex, sulfite displaces phosphate and binds to siroheme iron through sulfur. An extensive hydrogen-bonding network of positive side chains, water molecules, and siroheme carboxylates activates S-O bonds for reductive cleavage.

Sulfite and nitrite reductases (SiRs and NiRs) are key to both biosynthetic assimilation of sulfur and nitrogen and dissimilation of oxidized anions for energy transduction (1). Found throughout the three major kingdoms of living organisms (Archaea, Bacteria, and Eucarya), SiRs and most NiRs employ a siroheme (reduced porphyrin of the isobacteriochlorin class) (2) that is exchange-coupled with an iron-sulfur cluster to perform the remarkable reduction of a single atomic center by six electrons (3).

Assimilatory SiRs and NiRs in bacteria,

fungi, algae, and plants provide the reduced sulfur (oxidation state -2) and nitrogen (oxidation state -3) necessary for incorporation into biomolecules required by themselves and other higher organisms (1, 4). SiR generates sulfide from sulfite for subsequent cysteine biosynthesis in the terminal step of the 3'-phosphoadenylyl sulfate (PAPS) pathway (4). Assimilatory reduction of nitrate to ammonia proceeds by initial two-electron reduction to nitrite and then direct six-electron reduction to ammonia by an NiR that contains a siroheme and an iron-sulfur cluster (1). In contrast, dissimilatory denitrification transforms nitrate to nitrite, nitric oxide, nitrous oxide, and finally dinitrogen through sequential one- and two-electron reductions (1). The assimilatory chemistry is responsible for re-

ducing more than 10^4 megatons of NO₃⁻ a year, thus producing 100 times more NH₃ than nitrogen fixation by nitrogenase (5).

During dissimilatory sulfite reduction in sulfate-reducing eubacteria and some thermophilic archaeobacteria, sulfite can act as a terminal electron acceptor during anaerobic respiration (1, 4). Excess sulfide released to the environment contributes to biogeochemical sulfur cycling and causes corrosion and contamination problems for the oil and sewage treatment industries (6). Dissimilatory SiRs have siroheme and iron-sulfur clusters, are multimeric with varying subunit composition, and are differentiated from assimilatory sulfite reductases by their propensity to release trithionate (S₃O₆²⁻) and thiosulfate (S₂O₃²⁻) byproducts (1).

The *E. coli* assimilatory SiR (E.C. 1.8.1.2) is an oligomer of eight 66-kD flavoprotein (SiRFP) and four 64-kD hemoprotein (SiRHP) subunits (7, 8). In vivo, SiRFP transfers electrons from reduced nicotinamide adenine dinucleotide phosphate (NADPH) to SiRHP (9). Each SiRFP has one flavin adenine dinucleotide (FAD) and one flavin mononucleotide (FMN) binding site, yet the SiRFP octamer binds only four FAD and four FMN cofactors (8). Isolated SiRHP, when provided with suitable electron donors, can reduce SO₃²⁻ to HS⁻ and NO₂⁻ to NH₄⁺ without releasing intermediates (9, 10). In contrast, isolated siroheme catalyzes these reductions inefficiently and incompletely (11). SiRHP accommodates an electron at the siroheme with a redox potential (E'_0) of -340 mV (12), and at the Fe₄S₄ cluster with an E'_0 of -405 mV (13). Reduction of SiRHP enhances substrate binding and dissociation rates 10^5 times (10), suggesting a link between cofactor electronic states and protein conformation.

The crystal structures of SiRHP presented below reveal how a protein utilizes underlying twofold symmetry to associate cofactors and enhance their reactivity for catalysis. Conservation of chemically congruent residues between symmetry-related halves of SiRHP and among other SiRs and NiRs highlights segments of sequence nec-

B. R. Crane and E. D. Getzoff are in the Department of Molecular Biology, The Scripps Research Institute, La Jolla, CA 92037, USA. L. M. Siegel is in the Department of Biochemistry, Duke University Medical Center, Durham, NC 27710, USA.

*To whom correspondence should be addressed.

essary for stability and function and suggests that the topology of this sulfite or nitrite reductase repeat (SNiRR) persists in molecules as divergent as nitrate reductases and mammalian sulfite oxidases. Structures of the oxidized SiRHP active center in complex with phosphate to 1.6 Å resolution and in complex with the substrate sulfite to 2.2 Å resolution provide insight into the catalytic mechanism.

Structure determination and description. The crystallographic structure of SiRHP was solved by combining phase information from multiwavelength anomalous diffraction (MAD) (14) and multiple isomorphous replacement (MIR) plus anomalous scattering (MIRAS). Proteolytic cleavage produced the fully active hemo-protein species (residues 74 to 570) that was then crystallized (15). Extensive screening of heavy atom compounds (16) identified derivatives useful only at low resolution (Table 1) for supplementing the more powerful EMTS (ethyl mercurithiosalicylate) derivative (17). Secondary structural ele-

ments were built into MIRAS electron density maps, but large phase errors precluded further interpretation. MAD data (Table 2) were collected at three wavelengths chosen to maximize anomalous and dispersive signals from the five native iron atoms (18); combined phases derived from both MAD and MIRAS data produced an interpretable map. Difference Fourier analysis of a selenomethionine-substituted SiRHP (SeHP) aided sequence identification and chain tracing (19). Cycles of model-weighted phase combination, manual rebuilding with interactive graphics, and reciprocal space refinement (20) produced the final model (Table 3). Unexpected tetrahedral electron density at the distal axial coordination position of the siroheme in 1.6 Å resolution omit maps was modeled as a phosphate anion with due consideration to the crystallization conditions (15) and chemical environment (21).

In the SiRHP crystal structure, the siroheme, with bound phosphate, and the Fe₄S₄ cluster are juxtaposed at the interface of

three α/β mixed-sheet domains and bridged by a shared cysteine thiolate ligand (Fig. 1A). Viewed down onto the cofactors, the molecule is trilobed, approximately 60 Å in diameter and 40 Å thick (Fig. 1A). The central β sheet of each domain contributes to forming the interface between domains and to binding the prosthetic groups. Solvent-exposed helices pack around the periphery of the protein. A pseudo-twofold axis forms a single domain from subdomain 1 (residues 81 to 145) and subdomain 1' (residues 347 to 421, Fig. 1B), and relates domain 2 (residues 146 to 346, Fig. 1C) to domain 3 (residues 422 to 570, Fig. 1D). Thus, a previously unrecognized gene duplication apparently correlates an NH₂-terminal repeat (subdomain 1 plus domain 2 or residues 81 to 346) to a COOH-terminal repeat (subdomain 1' plus domain 3 or residues 347 to 570).

Subdomains 1 and 1' are related by pseudosymmetry to produce a topologically distinctive single domain resembling a parachute (Fig. 1B). The completely antiparal-

Table 1. Native and derivative data statistics. Derivative data sets were as follows: EMTS, 3-day soak in 0.1 mM ethyl mercurithiosalicylate; CH₃PbOAc, 2-day soak in saturated trimethyl lead acetate; 2HTPN, 6-day soak in 10 mM 2-hydroxyethane thiolate-(2,2',2''-terpyridine)-platinum nitrate; KAUCN₂,

cocrystallization of SiRHP with 4 mM potassium dicyanoaurate; CH₃HgOAc, 24-hour soak of 0.1 mM methyl mercury acetate and 0.2 mM thiomaleate; SeHP, selenomethionine substituted SiRHP (19). Native_{ano} and EMTS_{ano}, anomalous diffraction.

Data set	Resolution* (Å)	R _{merge} † (%)	σ _{cut}	Completeness (%)	R _{iso} or F _{ano} ‡ (%)	Phasing power§	R _C or R _K (%)	Sites¶ (No)
Native 1**	2.3 (2.5–2.3)	10.2 (19.7)	0	90 (52)				
Native 2††	1.6 (1.7–1.6)	9.9 (27.0)	0	97 (93)				
EMTS**	2.5 (2.7–2.5)	7.2 (14.3)	2	83 (43)	24.6	1.6	59	1
CH ₃ PbOAc‡‡	3.0 (3.2–3.0)	7.4 (10.7)	3	100 (100)	24.9	1.1	67	2
2HTPN‡‡	5.0	8.0	3	96	15.3	0.7	74	1
KAUCN ₂ ‡‡	5.0	9.5	3	100	15.3	1.2	61	2
CH ₃ HgOAc‡‡	5.0	12.6	3	95	23.9	1.4	61	4
SeHP§§	2.7 (2.9–2.7)	13.6 (35.5)	2	56 (34)	31.9	1.0	69	7
EMTS _{ano} **	3.5 (3.7–3.5)	5.8 (7.6)	1	88 (85)	6.4 (6.1)	1.1	15	6
Native _{ano}	2.5 (2.7–2.5)	10.5 (19.7)	1	98 (93)	8.1 (7.9)	1.9	13	5

*Highest resolution of data set followed by resolution range in highest bin for compiling statistics. †R_{merge} = Σ_i |I_i - ⟨I⟩| / Σ(I). |F| ≥ σ_{cut} × σ |F| used in heavy atom refinement and phasing. ‡R_{iso} = Σ ||F_{ph}| - |F_p|| / Σ |F_p| for isomorphous replacement (iso) data. F_{ano} = rms(|F⁺| - |F⁻|) / rms|F| for acentric anomalous scattering (ano) data (and for centric reflections) where rms is the root mean square. §Phasing power_{iso} = ⟨|F_{inc}⟩ / ⟨E⟩ where |F_{inc}| is the calculated heavy atom structure factor amplitude and E is the residual lack of closure error. Phasing power_{ano} = ⟨2|F_{ph}||⟩ / ⟨E⟩ where |F_{ph}|| is the anomalous correction component amplitude. ||R_C = Σ ||F_{ph}| ± |F_p|| - |F_{inc}|| / Σ ||F_{ph}| ± |F_p||, for centric reflections of isomorphous derivatives. R_K = Σ ||F_{ph}|| - |F_{phc}|| + ||F_{ph}|| - |F_{phc}|| / Σ |F_{ph}|| + |F_{ph}|| for anomalous scattering. ¶The number of heavy or anomalously scattering atoms. X-ray sources and instruments: **Dual Xuong/Hamlin proportional counter area detectors at University of California, San Diego (CuK_α); ††Mar Research image plate detector at the Stanford Synchrotron Radiation Laboratory (SSRL), beam line 7-1 (1.08 Å radiation); ‡‡Xentronics area detector, Elliott GX-21 rotating anode generator (CuK_α Ni-filtered radiation); §§Mar Research image plate detector, Elliott GX-21 rotating anode generator (CuK_α radiation); ||||Native anomalous signal taken from the average of the Bijvoet differences between Native 1 and a diffractometer data set collected at Duke University (17), reflections with ||F⁺| - |F⁻|| ≥ 2.0 × (||F⁺| - |F⁻||) removed.

Table 2. Multiwavelength anomalous diffraction statistics.

Wavelength (Å)	Completeness* (%)	R _{merge} † on F [±] (%)	Bijvoet signal‡		Dispersive signal§		f'	f''
			Calc. (%)	Obs. (%)	Calc. (%)	Obs. (%)		
a) 1.5418	93.0	5.6	1.9	5.7	vs. b) 1.8	vs. b) 3.5	-1.25	3.14
b) 1.7374	91.4	6.2	3.6	6.5	vs. c) 0.9	vs. c) 4.3	-5.98	4.73
c) 1.7412	90.0	5.3	2.4	5.7	vs. a) 2.7	vs. a) 5.2	-8.33	2.55

*Overall completeness of data to 2.5 Å resolution. †R_{merge} = Σ_i ||F_i[±]| - ⟨|F[±]||⟩ / Σ(|F[±]||) for comparison to calculated and observed signals. ‡Calculated Bijvoet signal = q(2f''), where q = (1/Z_{eff})(N_a/2N_p)^{1/2}; N_a is the number of anomalous scattering centers (5 Fe); N_p, the number of nonhydrogen enzyme atoms (4011 for SiRHP); and Z_{eff}, the effective normal scattering factor (~6.62 e). Observed Bijvoet signal = rms(Δ|F[±]||) / rms|F|. Errors estimated from symmetry-equivalent centric reflections give values of 1.5 to 1.7 percent. Observed signals are larger than those calculated due to correlated scattering of neighboring iron atoms at lower resolution (an increase of ~√N_a) and less attenuation of anomalous scattering, as compared to normal scattering, with higher resolution. §Calculated dispersive signal = qf'(λ₀) - f'(λ). Observed dispersive signal = rms(Δ|F[±]||) / rms|F|. f' and f'' are the real and imaginary components of the anomalous scattering vector in electrons (18).

lel β strands form an array of cords stretching upward from the harness turns (joining $\beta 3$ and $\beta 4$ of subdomain 1, and $\beta 3'$ and $\beta 4'$ of subdomain 1') to opposite ends of the four solvent-exposed canopy helices. When viewed through the central hydrophobic core, the two sheets and four helices form an almost equilateral triangle, directing the harness hairpins toward the interdomain interface and cofactor binding sites.

Domain 2 contributes residues for binding against its siroheme and chelating anions against its distal face, whereas domain 3 supplies the four cysteine Fe_4S_4 cluster ligands from the first two adjacent loop connections of its central β sheet (Fig. 1, C and D). These homologous domains are each constructed from a five-stranded mixed β sheet with $\beta 5(\beta 5')$, $\beta 6(\beta 6')$, and $\beta 7(\beta 7')$ parallel in their direction of propagation and $\beta 7(\beta 7')$, $\beta 8(\beta 8')$, and $\beta 9(\beta 9')$ antiparallel (parenthetical primed notations represent the symmetry-related structural elements). Each β sheet, linked entirely by nearest-neighbor connections, is flanked on its solvent-exposed side by parallel helices $\alpha 3(\alpha 3')$ and $\alpha 4(\alpha 4')$ and antiparallel helix $\alpha 5(\alpha 5')$. An extended 18-residue linker strand (residues 329 to 346) wraps 44 Å around the molecule to join the symmetry repeats (Fig. 1C).

Virtually all regions of the molecule contribute to binding and modulating the conformation of the cofactors or linker strand, either by direct contacts or by supplying a structural framework for those contacts to be made. The interface between domains 2 and 3 is formed by the spiral connection (type 1 turn linked to a 3_{10} helical turn) between $\beta 6(\beta 6')$ and

$\beta 7(\beta 7')$, the extended turn between $\beta 8(\beta 8')$ and $\beta 9(\beta 9')$, the second cluster binding loop (after $\beta 6'$), and the linker strand (Fig. 1, C and D). Side chains from the central spiral connections also make contacts with the cofactors and the parachute domain. The active-center architecture is constructed cooperatively from both symmetry repeats; one would be insufficient.

Twofold symmetry and the SNIrr. The SiRHP twofold symmetry provides compelling evidence for a new structural module, the SNIrr, which is common to a superfamily of anion redox enzymes. The

slight sequence conservation between the symmetry repeats, concentrated in four homology regions (H1 to H4), highlights residues imperative for form and function (Fig. 2A). The β strands of the two SiRHP symmetry repeats align well, whereas the positions, lengths, and conformations of helices and surface loops are more variable (Fig. 2B). One set of symmetry-conserved residues establishes and stabilizes local backbone conformation. Another set adopts chemical functions analogous to those found in the active center. Key structural determinants include (i) preferred glycines

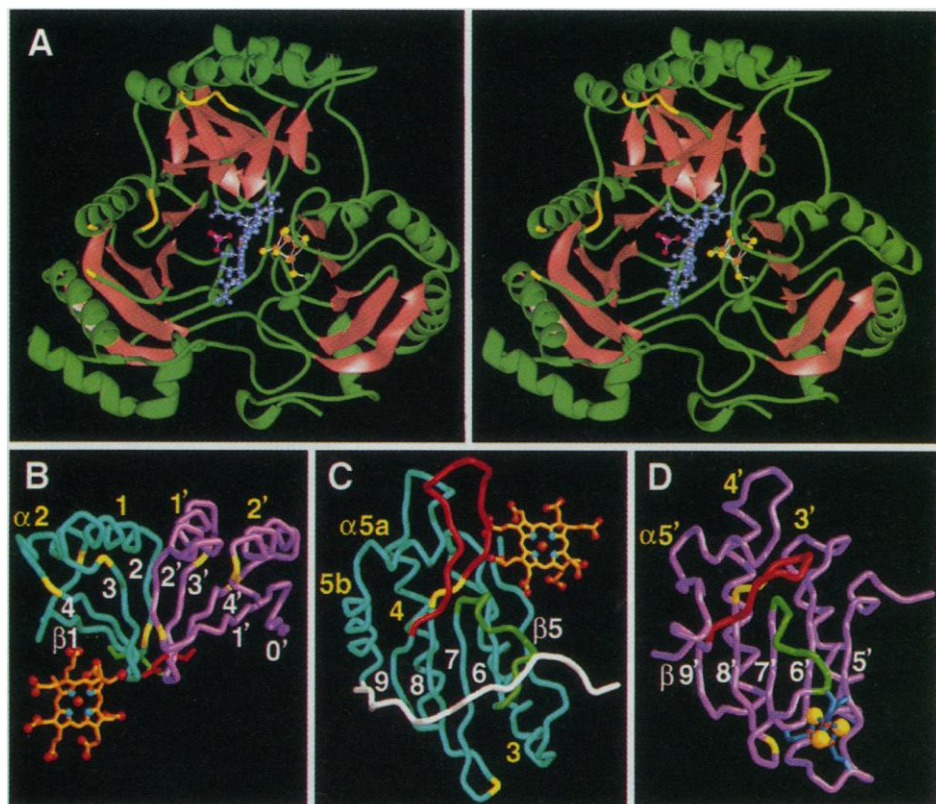


Fig. 1. Topology of SiRHP and its component domains. **(A)** Stereo view of the overall SiRHP fold with pseudo-twofold axis vertical. The siroheme (blue), Fe_4S_4 cluster (Fe, brown; S, yellow), and phosphate (purple and red) are bound in the active center at the interface of three domains: domain 1/1' (top), domain 2 (left of phosphate), and domain 3 (right of cluster). Disorder in the polypeptide chain (yellow coil) occurs in three surface loops (127–131, 184–209, and 146–148), all of which become more ordered in the sulfite complex. NH_2 -terminus, front, above the siroheme; COOH -terminus, lower right; α helices, green; β strands, red. **(B)** Parachute domain as α backbone tubes and siroheme (gold). Conserved glycines (yellow) between subdomain 1 (cyan) and subdomain 1' (magenta) have backbone conformations disfavored for other residues and help define the triangular shape of the parachute. Symmetry-related β sheets of subdomain 1 and 1' exchange end strands (2 and 2') to generate strand orders of 1, 4, 3, 2' and 0', 1', 4', 3', 2, where $\beta 0'$ of the COOH -terminal repeat corresponds to disordered residues 74–80 at the non-native NH_2 -terminus (Fig. 2A). Thr¹¹⁵ (green) and Thr³⁹³ (red) stabilize bulges in the harness turns by side-chain to main-chain hydrogen bonds, thereby allowing the Gln¹¹⁸ (green) and Gln³⁹⁶ (red) side chains to interact with the $\beta 5(\beta 5')$ main chain of domains 2 and 3. **(C)** Domain 2 and siroheme. Glycines conserved between domains 2 and 3 (yellow) guide local backbone conformation. The spiral connection between $\beta 6$ and $\beta 7$ (green) contributes to the interdomain interface and cofactor binding. The $\alpha 5_a$ helix, wedged perpendicularly between $\alpha 4$ and the 5-stranded β sheet, projects the extended turn between $\beta 8$ and $\beta 9$ (red) towards the symmetry-related half of the molecule. An extended strand (white) links $\alpha 5_b$ to $\beta 0'$, to join the symmetry repeats. **(D)** Domain 3 and Fe_4S_4 cluster. The cluster (Fe, brown; S, yellow) is ligated by Cys⁴³⁴ and Cys⁴⁴⁰ (first cluster loop connecting $\beta 5'$ to $\alpha 3'$) and by Cys⁴⁷⁹ and Cys⁴⁸³ (second cluster loop connecting $\beta 6'$ to the spiral connection). Colored tubes represent the symmetry-related regions described for domain 2 in Fig. 1C. (A) produced with RIBBONS (41); (B), (C), and (D) with AVS (42).

Table 3. SiRHP- PO_4^{3-} refined model statistics.

Scatterers	4186	
Residues		
Total	456	
Two conformers	4	
Disordered	41	
Cofactors	1 Siroheme	1 Fe_4S_4
Ions	1 HPO_4^{2-}	1 K^+
Waters (No)	486	
Resolution (Å)	10.0–1.6	(1.67–1.6)*
Reflections (No)	61005	(7058)*
$\langle I/\sigma \rangle^\dagger$	28.7	(7.5)*
R factor ‡ (%)	19.1	(29.4)*
Free R § (%)	21.8	(30.0)*
(Protein B) (Å ²)	16.9	(9.7)
(Water B) (Å ²)	39.0	(17.3)
Rmsd bonds ¶ (Å)	0.010	
Rmsd angles ¶ (°)	1.6	

*Highest resolution bin for compiling statistics. † Intensity signal-to-noise ratio. $^\ddagger R = \sum | |F_{\text{obs}}| - |F_{\text{calc}}| | / \sum |F_{\text{obs}}|$ for all reflections (no σ cutoff). § Free R (40) calculated against 10 percent of the reflections removed at random after the model was completed. After releasing the selected data, positional and thermal (B) factor refinements were carried out until the R factor leveled, producing the tabulated value. ¶ Estimated standard deviation in B factors. ¶ Root-mean-square deviations from bond and angle restraints.

that allow main-chain conformations otherwise prohibited by local side-chain collisions, and (ii) conserved side-chain to main-chain hydrogen bonds that stabilize turns and transitions between secondary structural elements. Side chains that hydro-

gen bond to main chain may be preserved because their mutation could leave the hydrogen-bonding potential of the invariant peptide backbone unfulfilled in the absence of conformational change. Conservation of the SiRHP homology regions among other

SiRs and NiRs (Table 4) defines the SNIiRR and indicates a conserved twofold-symmetric catalytic unit despite variation in size and oligomeric state.

Region H1 forms a β hairpin, which is composed of $\beta 3(\beta 3')$, the harness turn, $\beta 4(\beta 4')$, and two flanking glycines (Fig. 2B) and conserves structural features obligatory for the three-dimensional shape of the parachute domain (Fig. 1B). H2, including $\beta 5(\beta 5')$ and the subsequent loop, and H3, including $\beta 6(\beta 6')$, the subsequent loop, and its following spiral connection, conserve residues acting in cofactor and substrate binding as well as their symmetry analogues, suggesting an ancestral dimer with two active centers. In the SiRHP NH_2 -terminal SNIiRR, H2 and H3 have lost Fe_4S_4 cluster binding functionality, whereas in the COOH-terminal SNIiRR, H2 and H3 have lost anion binding functionality. Nevertheless, some apparently vestigial cofactor and substrate-binding residues have been maintained and recruited for structural interactions (Fig. 2A). Region H4 contains conserved glycines and other structural determinants that direct the extended loop between $\beta 8(\beta 8')$ and $\beta 9(\beta 9')$ toward the center of the molecule to stabilize siroheme binding and the interface between domains 2 and 3 (Fig. 3A).

The persistence of active center features in the symmetry-related region of the molecule is exemplified by the long linker joining the SNIiRRs (Fig. 3A). Region H5, at the COOH-terminal end of the linker, is a seven-residue segment, conserved among some SiRs and NiRs, that binds into the residual invagination symmetry-related to the active center and forms a structural mimic for siroheme (Fig. 3B). The siroheme-bound anion is also mimicked by the linker, suggesting that both contribute to molecular stability. Stabilization by the linker strand, through excluded surface area and buried hydrogen bonds, may primarily prevent conformational flexibility since the association of the SNIiRRs alone sequesters sufficient surface area for a stable dimeric association (22).

Structural implications for the SNIiRR superfamily. Together, the first four SNIiRR homology regions and the separations between them are conserved in sequences from highly divergent organisms (Table 4). H2 to H4 are often tandemly repeated, presumably to generate a pseudodimer. These sequence preferences represent important structural and functional constraints for the SNIiRR, even though the two SiRHP SNIiRRs no longer share the same cofactor-binding constraints.

Tandem SNIiRRs (each containing H1 to H4 separated by one H5) are shared by the assimilatory sulfite (SynaSiR, 70 kD) and nitrite reductases (SynaNiR, 56 kD) from

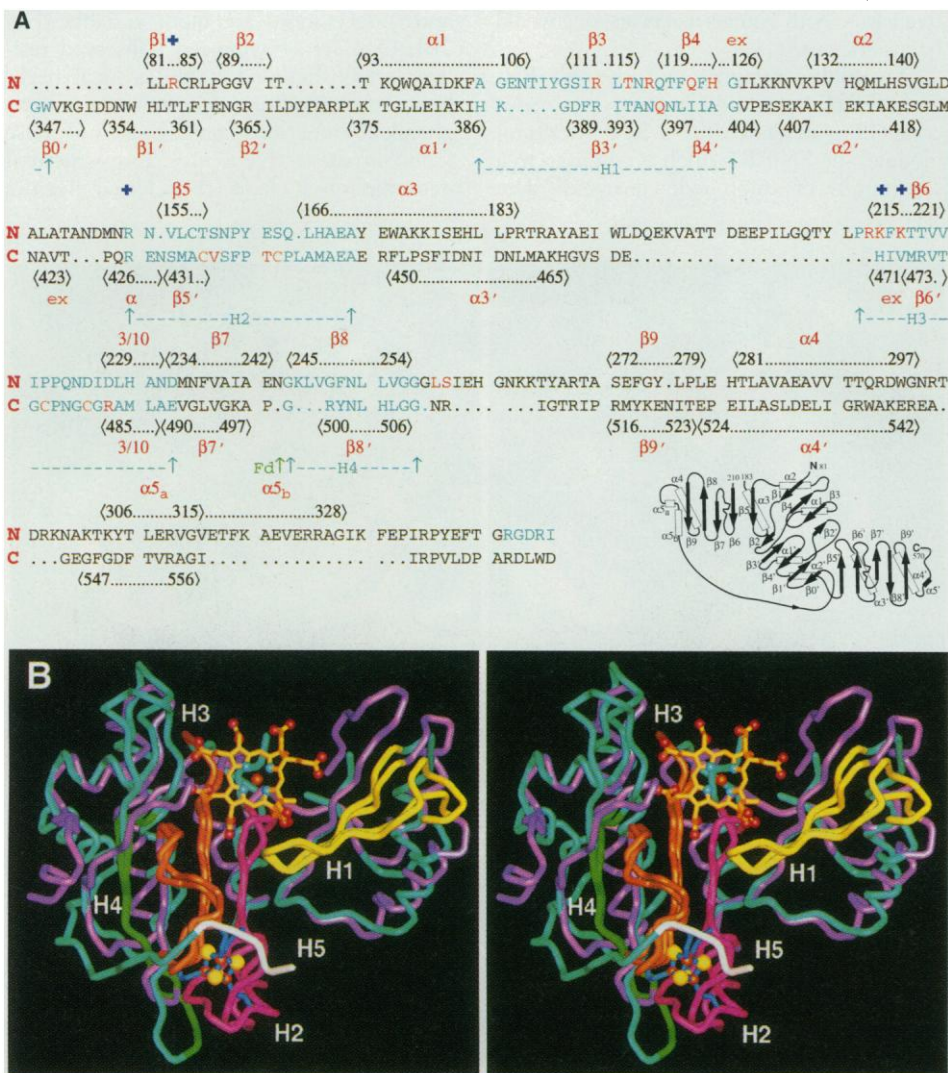


Fig. 2. SiRHP symmetry defines the SNIiRR. **(A)** In a sequence alignment based on structural superposition (see Fig. 2B), NH_2 -terminal (above) and COOH-terminal (below) SiRHP SNIiRRs have 17% residue identity. Residues (one letter code) are numbered at either end (()) of secondary structural elements, β strand extensions (ex), and spiral connections (3/10). Residues that bind the siroheme carboxylates (red), the Fe_4S_4 cluster (gold), and the phosphate (blue crosses) are indicated. The homology regions (cyan) found between the symmetry repeats and among related SiR and NiR sequences are underscored H1 to H5. Locations of insertion points for domains supplying reducing equivalents in other SiRs or NiRs (Table 4) are mapped onto the SiRHP sequence: Fd, ferredoxin-like domain in ArfSiR; Fv, flavodoxin-like domain in AnaNiR and EcdNiR. Inset - Twofold symmetric topology of SiRHP (rectangles - α helices, arrows - β strands, bent line - 3_{10} helix). The SNIiRR formed by subdomain 1 (upper center) and domain 2 (upper left) is twofold symmetric with the SNIiRR formed by subdomain 1' (lower center) and domain 3 (lower right). The surface-exposed loop between $\alpha 3$ and $\beta 6$ (184-209) is disordered (43). The first ordered residue at the proteolytically cleaved NH_2 -terminus is 81. **(B)** Superposition of the NH_2 -terminal SNIiRR (cyan) with associated siroheme (gold) and the COOH-terminal SNIiRR (magenta) with associated Fe_4S_4 cluster (Fe, brown; S, yellow; cysteine thiolates, blue) shown in stereo as $\text{C}\alpha$ backbone tubes (42). SiRHP homology regions [H1, yellow; H2, pink; H3, orange; H4, green; H5, white; see (A)] are mapped onto both SNIiRRs. In subdomains 1 (81-145) and 1' (347-421), the crossover β strands $\beta 1(\beta 1')$ - $\beta 2(\beta 2')$ (81-90, 357-366) and the harness β hairpins $\beta 3(\beta 3')$ - $\beta 4(\beta 4')$ (110-118, 388-396) superimpose with a root-mean-square deviation (rmsd) of 0.8 Å for 19 matched $\text{C}\alpha$ s. In domains 2 (146-346) and 3 (422-570) $\beta 5(\beta 5')$ (155-158, 431-434), $\beta 6(\beta 6')$ (215-221, 471-477), the spiral connections and $\beta 7(\beta 7')$ (229-241, 485-497), $\beta 8(\beta 8')$ (248-253, 500-505), $\beta 9(\beta 9')$ (272-276, 516-520), and $\alpha 5(\alpha 5_a')$ (306-315, 547-556) superimpose with an rmsd of 1.5 Å for 45 matched $\text{C}\alpha$ s.

the cyanobacterium *Synechococcus* (23) and the homologous spinach assimilatory NiR (SpiaNiR, 53 kD) (23, 24). These three monomeric enzymes all derive reducing equivalents from ferredoxin. The much larger NiRs from *Aspergillus nidulans* (AnaNiR, 88 kD) and *E. coli* (EcdNiR, 120 kD) have no detectable H5 region but instead contain inserted flavin-binding domains (23). The homologous subunits of the $\alpha_2\beta_2$ tetrameric dissimilatory SiR from the thermophilic archaeobacterium *Archaeoglobus fulgidus* (ArfdSiR, $\alpha 47$, $\beta 41$ kD) each contain a single SNiRR as well as an inserted ferredoxin-like Fe_4S_4 -binding domain to supply reducing equivalents (23). The β subunit contains H5, but lacks a cluster ligand, suggesting that ArfdSiR functions as two α/β heterodimers, each with a single active center. The small assimilatory-like SiR from *Desulfovibrio vulgaris* (DvaSiR, 25 kD) is apparently monomeric (23, 25), but only contains a single SNiRR. In the context of a SNiRR fold, the observed exchange coupling between cofactors (3) requires DvaSiR to form a twofold symmetric homodimer that assembles two active centers.

A single SNiRR also appears in the molybdopterin cofactor-binding domains of assimilatory nitrate reductases from plants (AtNR) (23) and fungi, which catalyze the initial two-electron reduction of nitrate to nitrite in nitrogen assimilation (1), and in the related mammalian sulfite oxidases, which oxidize sulfite to sulfate in the degradation of cysteine and methionine (RatSO) (23). Moderate conservation of ligand-binding residues and $\text{C}(X)_5\text{C}$ spacing between plant nitrite and nitrate reductases suggests that SNiRRs bind molybdopterins to mediate a cofactor-assisted homodimeric assembly (1). These homology relations extend the SNiRR fold to a superfamily of distantly related redox enzymes that includes molecules in virtually all living organisms.

SiRs and NiRs require reducing equivalents for activity. In *E. coli* SiR, four pseudosymmetric SiRHPs bind eight SiRFPs with only half of their 16 flavin binding sites occupied. Extreme negative cooperativity in SiRFP may be either the evolutionary cause for directed electron transfer to a preferred active center of a once dimeric SiRHP, or the adaptive result of binding a gene-duplicated pseudosymmetric SiRHP containing a single active center. Only one pseudosymmetric molecular face (the exposed helices of the parachute) is available for SiRFP binding, as the other is blocked by the COOH-terminus (Fig. 3A). A pair of negatively charged, 66-kD SiRFPs (8, 9) could simultaneously and pseudosymmetrically interact with the helices of the parachute domain, allowing one SiRFP to bind the positive electrostatic surface surrounding the

active-site cavity (Fig. 4). Here, tryptic cleavages of SiRHP at the NH_2 -terminus and the $\alpha 3$ to $\beta 6$ loop are prevented in the holoenzyme (data not shown). In ArfdSiR, the ferredoxin-like domain inserted between $\beta 7'$ and $\beta 8'$ (Fig. 2A) would sit above the positive surface, close to the only completely exposed aromatic residue, Phe⁴³⁸, on the first cluster binding loop.

Active-center cofactor coupling. In SiRHP's active center, the distal axial co-

ordination site of the siroheme has been optimized for binding substrate anions, whereas the proximal site is occupied by a covalently bound thiolate from Cys⁴⁸³, which also acts as a ligand to the Fe_4S_4 cluster (Fig. 5A). Siroheme (Fig. 5B) has two adjacent, saturated pyrrole rings (rings A and B) and two adjacent, unsaturated pyrrole rings (rings C and D). Low temperature Mössbauer (3), optical (13), EPR (electron paramagnetic resonance)

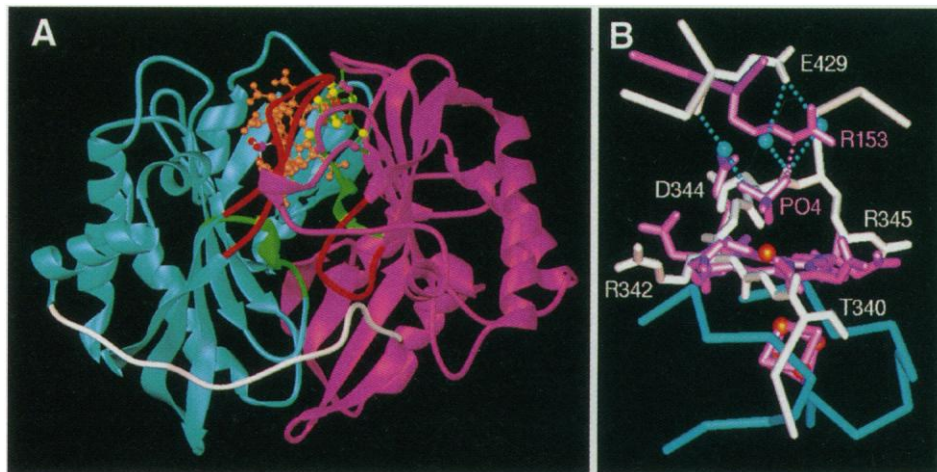
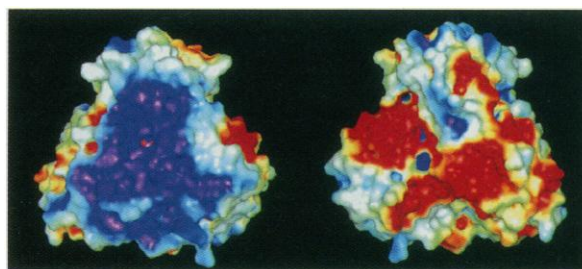


Fig. 3. SiRHP as a pseudodimer. **(A)** SiRHP fold and secondary structure viewed down the pseudo-twofold axis toward the parachute domain. NH_2 -terminal (cyan) and COOH -terminal (magenta) symmetry repeats are linked by an extended strand (329–346; white). The spiral connections (229–234, 485–490; green) and the extended turns (red) between $\beta 8(\beta 8')$ and $\beta 9(\beta 9')$, along with the parachute domain (beneath), participate in the interface formed by the dyad. The siroheme (gold) and bound phosphate (purple and red) are mimicked by the linker loop's COOH -terminal end (340–345) which inserts into a vestigial pocket (bottom), symmetry related to the active center. The COOH -terminus forms a distorted helical turn that packs in front of, and between, $\beta 9$ and $\beta 9'$. Produced with RIBBONS (41). **(B)** Molecular mimicry of the siroheme by the linker strand. Residues 340–345 of the linker strand act as an analogue for ligand-bound siroheme within a cavity symmetry-related to the active center, and embody a well-adapted peptide inhibitor. The active-center siroheme, Fe_4S_4 cluster, phosphate, and Arg¹⁵³ (magenta) were transformed by the operation that superimposed domains 2 and 3 in Fig. 2B. Residues symmetry-equivalent to siroheme-binding residues interact with linker strand functional groups symmetry-equivalent to siroheme functional groups (white). Asp³⁴⁴ superimposes on the siroheme's most axial propionate and mimics its interaction with the harness turn of subdomain 1 by hydrogen bonding to the harness turn of subdomain 1'. Hydrogen bonds from water molecules (cyan) to Glu⁴²⁹ (top) and the backbone of Asp³⁴⁴ imitate the interaction between Arg¹⁵³ and the bound phosphate anion. The transformed Fe_4S_4 cubane resides in a hydrophobic core between the cluster-loop analogs in domain 2 (cyan), indicating that a primordial dimeric SiRHP could have accommodated a second active center. Modeled with InsightII (Biosym Technologies, San Diego, California).

Fig. 4. Electrostatic potential mapped onto SiRHP's solvent-accessible molecular surface. In the left orientation (matching Fig. 1), the active center (phosphate ball and stick model partially visible in center) is surrounded by significant positive (blue) electrostatic potential, while the symmetry-related face of SiRHP (right view, 180° rotated about the vertical pseudo-twofold axis) is more negative (red). The electrostatic potential (contoured at $3/2 kT/q$; k = Boltzmann constant, T = temperature, q = 1 point charge) was calculated with the Poisson-Boltzmann equation as implemented in Delphi (44) using formal charges (phosphate anion removed, internal dielectric constant = 2.0, external dielectric = 80.0, ionic strength = 0.145 M, grid space = 1.3 Å). To avoid discontinuities at the protein-solvent boundary, the potential was sampled 2.6 Å from the solvent-accessible surface [calculated with MS (22), 1.4 Å probe radius] and then mapped back onto the surface. Rendered in AVS (42).



(13), ^{57}Fe ENDOR (electron-nuclear double resonance) (26), Soret band excited resonance Raman spectroscopy (27), paramagnetic-shifted NMR (nuclear magnetic resonance) experiments (28), and preliminary crystallographic studies (17) are all consistent with the observed covalent bridge between the siroheme iron and Fe_4S_4 cluster. The 2.84 Å bond between the ferric siroheme iron (spin quantum number $S =$

5/2) and the Sy of Cys^{483} is unusually long, which agrees with weak Fe-to-Fe exchange-coupling predicted by computational models based on Mössbauer spectroscopy (29). The siroheme iron and cluster iron (Fe_4) bridged by $\text{Cys}^{483}\text{Sy}$ are 4.48 Å apart and form a 126° Fe-Sy 483 -Fe angle. The closest noncovalent separation between the cofactors, a 3.63 Å van der Waals contact between Fe_4S_4 inorganic sulfur (S1) and the

meso carbon separating the pyrroline rings (CHB), presents a possible auxiliary electron transfer pathway.

The Fe_4S_4 cubane is bound by four cysteine thiolates (Fig. 5A), which are supplied in pairs from the cluster loops immediately succeeding the first two parallel β strands of domain 2 (Fig. 1C). The separation between ligands in each loop, CX_2C for the first and CX_3C for the second, is the most conserved sequence pattern throughout the family of related SiRs and NiRs. SiRHP may stabilize the cluster's ferredoxin-like, +2/+1, low potential redox couple (-405 mV) by delocalizing negative charge through hydrogen bonds from local protein amide linkages and by controlling accessibility to solvent. The Fe_4S_4 cubane lies only 5.1 Å beneath the solvent-accessible surface, and Cys^{479} Sy presents 7.7 Å² of exposed surface area, allowing cluster solvation. The cluster loops also supply six main-chain and two side-chain hydrogen bonds to the Fe_4S_4 cluster. The cluster approximates typical D_{2h} symmetry but exhibits subtle distortions involving the iron bound to Cys^{483} Sy, which may have implications for electronic coupling to the siroheme (30).

The SiRHP protein scaffold selects for and fixes the saddle-shaped distortion of the siroheme (S_4 point symmetry) (Figs. 5 and 6). Relatively large dihedral angles between opposite pyrrole or pyrroline rings pucker the isobacteriochlorin meso carbons CHD, and, more drastically, CHB, down toward the cluster allowing the van der Waals contact between CHB and cluster S1 (Figs. 5 and 6). The nonplanarity of the saturated pyrroline rings is coupled to the orientations of their attached carboxylates. The protein organizes extensive hydrogen bonding networks to recognize these pyrroline carboxylates, which are much more axial than their pyrrole counterparts (Fig. 6). Stabilization of a siroheme π -cation radical by the SiRHP active center architecture may favor concerted reduction by three electrons and lessen the need to stabilize bound intermediates. Relative to other porphyrin derivatives, isobacteriochlorins have destabilized HOMO orbitals (of a_{1u} symmetry) because of the reduced delocalization of the saturated pyrroline rings (31). Extensive S_4 ruffling of the SiRHP siroheme, coupled with charge-transfer from the associated electron-rich Fe_4S_4 cluster, should further destabilize the macrocycle HOMO and increase the efficacy of ring oxidation.

Anion recognition and catalysis. A remarkable array of positively charged side chains coordinates anions bound to the siroheme, providing them with a strong polarizing environment and high effective proton concentration (Fig. 6). The entire

Table 4. Five homology (H) regions common to a representative group of SiR and NiRs. For enzymes with a tandem repeat, the NH_2 -terminal sequence range precedes the COOH -terminal range in each homology region. Average separations between homology regions (excluding the inserted ferredoxin-like cluster domain of ArfdSiR) are 28.2 (3.3) residues for H1-H2, 24.6 (13.0) for H2-H3, and 8.1 (2.1) for H3-H4 (estimated standard deviation in parentheses).

Enzyme	H1†		H2		H3		H4		H5
SiRHP*	103-124	386-402	153-171	428-448	213-234	471-490	244-255	499-507	342-348
SynaSiR	93-113	393-416	142-159	441-459	222-243	480-502	254-265	507-519	305-312
DvaSiR	39-60		86-104		121-142		151-158		
ArfdSiR $_{\alpha}$	112-135		171-189		210-223		307-314		
ArfdSiR $_{\beta}$	74-94		129-147		168-189		263-270		325-329
SynaNiR	87-109	341-363	138-156	391-409	181-202	429-448	212-222	460-472	303-309
SpiaNiR	161-182	417-439	211-229	468-486	254-275	506-525	285-295	538-550	379-385
AnaNiR	157-187	657-686	221-236	715-733	275-296	750-771	303-311	780-787	
EcdNiR	113-143	578-607	172-187	632-651	226-247	670-691	254-262	700-707	
AtNR	152-193		221-248		262-285		295-308		
RatSO	168-209		237-263		273-298		305-318		

*Assimilatory SiRs: SiRHP, *E. coli* GenBank accession No. M23008 (8); SynaSiR, *Synechococcus cyanobacterium*, Z11755; DvaSiR, *Desulfovibrio vulgaris*, M77241. Dissimilatory SiRs: ArfdSiR, *Archaeoglobus fulgaris*, α and β subunits, M95624. Assimilatory NiRs: SynaNiR, *Synechococcus cyanobacterium*, M95624; SpiaNiR, spinach, X67680; AnaNiR, *Aspergillus nidulans*, M58289. Dissimilatory NiR: EcdNiR, *E. coli*. Nitrate reductase: AtNR, *Arabidopsis thaliana*, J03240. Sulfite oxidase: RatSO, rat, L05084. †H1, Ala-(X) $_{5-7}$ - ϕ -Gly-(X) $_{2-6}$ -p-X-Thr-X-p-Gln-X-n-X-n-X-Gly; H2, Arg-X-n-(X) $_2$ -Cys-(X) $_5$ -Cys-(X) $_4$ -Asp/Glu-Ala/Ser/Thr; H3, Pro-Arg-Lys- ϕ -Lys/Asn/n-(X) $_{1-4}$ -Gly-Cys(X) $_3$ -Cys(X) $_{6-8}$ -Asp/Glu; H4, Gly-(X) $_{4-8}$ -Val/Leu/Ile-Gly-Gly; H5, Arg-Gly-Glu/Asp-Arg/Lys-Ile-Gly- ϕ , where n is a nonpolar residue, p is a polar residue, ϕ is an aromatic residue, and residue ranges are approximate. For sequence citations see (23).

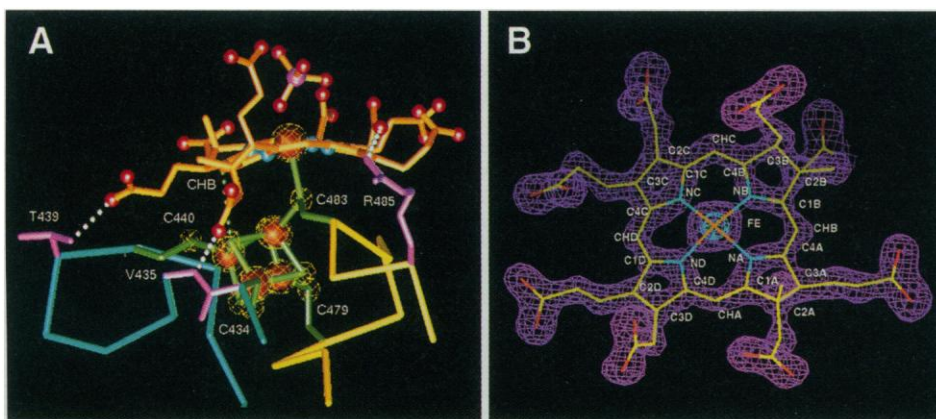


Fig. 5. SiRHP's active center. **(A)** Cofactor coupling. The model is shown with a 1.6 Å resolution, simulated annealed, $F_o - F_c$, σ_A -weighted (45) omit electron density map (46), calculated with the Fe_4S_4 cluster, cysteine ligands, and siroheme removed from the refinement and phase calculation. Solid brown contours (24 σ) identify iron positions while basket yellow contours (16 σ) mark both sulfur and iron positions (0.4 Å grid spacings). Four cysteine thiolates ligate the cluster (green bonds): Cys^{434} , Cys^{440} (cyan $\text{C}\alpha$ trace), Cys^{479} , and Cys^{483} (yellow $\text{C}\alpha$ trace). The siroheme (gold bonds) and cluster share a thiolate ligand from Cys^{483} and contact one another through a van der Waals interaction (green dotted line) between siroheme CHB cluster inorganic sulfide S1. Hydrogen bonds (white dotted lines) between the siroheme carboxylates (oxygens shown as red spheres) and cluster binding loop residues (magenta) aid cofactor association and domain integration. Phosphate is bound through its oxygen in the distal axial siroheme coordination site. **(B)** Siroheme structure and electron density. The 1.6 Å resolution, σ_A -weighted, $F_o - F_c$ omit electron density map was calculated with the siroheme removed, and contoured at 30 σ (cyan) and 5 σ (purple) (0.4 Å grid spacings). The siroheme's saddle shape (yellow, carbon; blue, nitrogen; red, oxygen bonds) results from the saturated pyrroline rings and approximates S_4 point symmetry. Each pyrroline (A and B) or pyrrole (C and D) ring has one acetate and one propionate at the 2 and 3 positions, while the pyrroline rings have an additional methyl group. (A) displayed in AVS (42), (B) displayed in XFIT (47).

active-site cleft is solvated by ordered water molecules, which form complicated hydrogen bonding networks among the siroheme carboxylates, charged active-site residues, and bound anions. The surprising and unprecedented binding of phosphate to the porphyrin, through a 1.85 Å Fe-O bond and 136° Fe-O-P angle, likely represents a weak-field σ -bonding interaction between the iron and oxygen lone pair. S_4 ruffling increases the siroheme core size, which accommodates the large, high-spin, ferric iron with a relatively small (0.29 Å) displacement above the least-squares plane of the pyrrole and pyrroline nitrogens (32). The bound phosphate anion stabilizes and complements the positively charged side chains concentrated in the active center, suggesting that exchange of kinetically trapped anions may account for the 10^5 -fold reduction in substrate and inhibitor binding rates relative to reduced SiRHP (10).

A 2.2 Å resolution structure of the oxidized SiRHP-sulfite complex reveals significant changes from the phosphate-bound structure only at the active center and surrounding loops (33). The trigonal-pyramidal sulfite binds the ferric siroheme iron via its sulfur with a siroheme Fe-S bond distance of 2.26 Å (Fig. 7). Reflecting the observed transition from high ($S = 5/2$) to low ($S = 1/2$) spin (34), the ferric iron resides only 0.09 Å above the least-squares plane of the pyrrole and pyrroline nitrogens, a ~ 0.2 Å movement into the plane when compared to the phosphate complex. This lessened doming, resulting from an unoccupied iron $d_{x^2-y^2}$ orbital and thus a smaller iron radius, reduces the bond length between the bridging thiolate and siroheme iron from 2.84 to 2.46 Å and thereby likely increases the cofactor coupling. A slight flattening of the siroheme produces a closer van der Waals contact (3.53 Å) between cluster S1 and siroheme CHB. Exchange of phosphate for the substrate sulfite is accompanied by ordering of three active-center proximate loop regions (Fig. 1) and rearrangements of active-site side chains and solvent molecules. Variable ligand-binding geometries indicate that torsional freedom available from long, extended, active-center side chains, coupled with changing water structure, allows the enzyme to stabilize catalytic intermediates at different stages of oxygenation. The loop and side-chain movements also suggest that kinetic trapping of anions by the oxidized enzyme may reflect a slow conformational step.

Although many heme proteins react with nitrite, only siroheme and siroheme proteins have been shown to react significantly with sulfite (11, 35). The preference for siroheme to bind and reduce sulfite probably depends on the partial saturation and flexibility of the isobacteriochlorin ring. The partial satura-

tion increases the electron-donating ability of the heme cofactor, promoting both more stable bonding with a sulfite π -acid ligand and destabilization of the macrocycle HOMO to the point of possibly involving a siroheme cation radical in catalysis. The greater conformational flexibility allows nonplanarity and S_4 ruffling which (i) also affects the stability of the frontier orbitals, (ii) leads to a van der Waals contact between the siroheme and cluster, possibly relevant for electron transfer or stabilization of a macrocycle radical species, and (iii) directs displacement of the siroheme iron during transitions from high- to low-spin.

The SiRHP distal substrate binding site is exquisitely designed to perform electrophilic or general acid catalysis. Because of sulfur-oxygen charge separation, sulfite S-O semi-ionic bonds are extremely short, stable, and resistant to polarization when compared to those of other sulfur-oxygen species (36). Oxygen protonation greatly weakens S-O bonds through polarization and dissipation of ionic character (36). Active-site Arg and Lys residues likely act as general acids to directly protonate substrate or activate water to do so. The enzyme-bound sulfite appears singly protonated (HSO_3^-) as one S-O bond consistently refines ~ 0.2 Å longer than the other two. The protonated oxygen (O3) also appears to be a proton acceptor in a hydrogen bond

from an ordered water molecule, since this same water also hydrogen bonds to the proton donors Arg¹⁵³ and Lys²¹⁵. Given the solution pK_a of 6.9 for the equilibrium between HSO_3^- and SO_3^{2-} (37), the apparent presence of HSO_3^- in the crystals at pH 7.9 (the pH optimum for sulfite reduction by SiR) (7) suggests that SiRHP's active center promotes sulfite protonation and thereby progression toward formation of a favorable water or hydroxide leaving group. Charge flow from siroheme into the sulfur 3d orbitals (made possible by sulfite binding through sulfur to siroheme iron) would reduce the positive character of the sulfur and propagate electron density to S-O 3d-2p π^* -antibonding orbitals, both weakening the ionic and covalent bonding systems and increasing the negative charge of sulfite oxygens to further facilitate protonation and bond breaking. Two water molecules associate with all three sulfite oxygens, and one forms a ~ 2.6 Å hydrogen bond with 3 σ bridging difference density to sulfite O3 (Fig. 7). This may anticipate an early stage of the reaction where oxygen O3 is further protonated and reductively cleaved.

SiRHP may be representative of an ancient ancestral enzyme involved in early multi-electron reductions of inorganic substrates. Biological sulfate reduction is the only process that can generate sulfide from sulfate at ambient temperatures and pres-

Fig. 6. Distal anion binding site. Positive side chains (magenta bonds with blue nitrogen atoms) Arg⁸³ ($\beta 1$), Arg¹⁵³ ($\beta 5$), Lys²¹⁵ ($\beta 6$), and Lys²¹⁷ ($\beta 6$) extend from their respective β strands (cyan with red oxygen atoms) to coordinate the siroheme-bound phosphate (yellow and red bonds). $\beta 6$ is stabilized by salt bridges between Arg²¹⁴ and both pyrrole ring D carboxylates, and the insertion of Phe²¹⁶ into a hydrophobic core. Arg¹¹⁷ hydrogen bonds to the $\beta 5$ and $\beta 6$ main chain, forms a wall of the cavity, and buttresses Arg⁸³ for a close contact with bound anions. The most axial siroheme propionate interacts with the Asn¹⁵⁴ main chain (upper right) through a bridging water molecule (blue sphere), and is in hydrogen bonding distance to O2, which appears to be protonated due to a P-O2 bond length that refined 0.2 Å longer than the other P-O bonds. The only solvent-exposed phosphate oxygen (O4) hydrogen bonds to an ordered water molecule sitting 2.7 Å away in a solvated channel that leads out of the active-site cavity (see Fig. 4). Rendered in AVS (42).

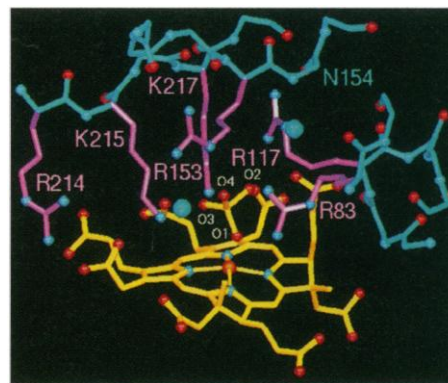
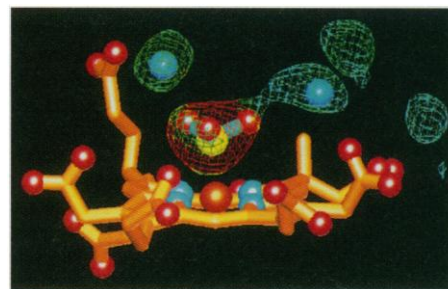


Fig. 7. Electron density for siroheme-bound sulfite and interacting water molecules. The 2.2 Å resolution, σ_a -weighted, $F_o - F_c$ omit map (0.24 Å grid spacings) of the sulfite complex was calculated before addition of a distal ligand or active-site water molecules. Basket contours (3 σ) are colored by the electron density gradient (maximum to minimum: red to yellow to green to blue). The trigonal-pyramidal peak (small, yellow and green gradient at its four corners) is fit well by a sulfite molecule bound to the siroheme through sulfur. Electron density bridges from the longest S-O bond to a water peak (blue) 2.6 Å away. Displayed in AVS (42).



tures. The anaerobic ecosystem established by the sulfate-reducing bacteria and their photolithotrophic and chemolithotrophic counterparts provided one of the first biological contributions to biogeochemical cycling (38). As dissimilatory sulfite reduction existed 2350 to 3100 million years ago (38), at least 1 billion years before the advent of a significantly oxidizing environment (39), this chemistry likely predated cytochrome-based aerobic respiration. Siroheme may be the ancestor of cytochrome cofactors as it is derivable from early intermediates in heme synthesis, and it would be more stable than unsaturated porphyrins to the photoreducing environment of the Archean world (2, 4). The obligate anaerobe *Clostridium pasteurianum*, which has characteristics of archaic heterotrophs, contains no cytochromes, yet does have a sulfite reductase (2, 4). Thus, the original sulfur-based anaerobic respiratory systems, which were under evolutionary pressure to utilize oxidized sulfur compounds for redox couples rather than to produce sulfide, are the likely progenitors of contemporary assimilatory SiRs and NiRs, and also possible evolutionary vehicles for the later development of heme-dependent respiratory oxidases.

The appearance of the SNI_{RR} superfamily throughout the diversity of life suggests that conservation of the SNI_{RR} structural framework and overall twofold pseudosymmetric catalytic unit has been paramount for efficacious cofactor assembly. The development of SiRHP from an ancient dimer may be a common theme in multi-cofactor enzyme evolution where initial homodimer formation can reinforce symmetric mutations to facilitate adoption of a general functionality (co-factor binding at an interface), and then gene duplication to a pseudodimer can allow mutations to optimize asymmetric features under the constraint of the original functionality. Mutations advantageous for one operative (siroheme binding) would likely no longer be detrimental for another that previously relied on the same scaffolding (cluster binding). In SiRHP, two divergent SNI_{RR}s create a microenvironment at their interface to modulate cofactor reactivity, carefully control solvation and protonation, and electrostatically stabilize transition states for high fidelity generation of fully reduced product—an achievement not attained by model systems, isolated cofactors, or the dissimilatory enzymes.

REFERENCES AND NOTES

- J. A. Cole and S. J. Ferguson, Eds., *Forty-Second Symposium of the Society for General Microbiology: The Nitrogen and Sulphur Cycles* (Cambridge Univ. Press, Cambridge, 1988); J. L. Wray and J. R. Kinghorn, Eds., *Molecular and Genetic Aspects of Nitrate Assimilation* (Oxford Science Publications, Oxford, 1989).
- M. J. Murphy and L. M. Siegel, *J. Biol. Chem.* **248**, 6911 (1973).
- J. A. Christner, E. Münck, P. A. Janick, L. M. Siegel, *ibid.* **258**, 11147 (1983); I. Moura et al., *J. Am. Chem. Soc.* **110**, 1075 (1988); B. H. Huynh, L. Kang, D. V. DerVartanian, H. D. Peck Jr., J. LeGall, *J. Biol. Chem.* **259**, 15373 (1984).
- L. M. Siegel, in *Metabolic Pathways* (Academic Press, New York, 1975), vol. 7, pp. 217–286; H. D. Peck Jr. and T. Lissolo, in *Forty-Second Symposium of the Society for General Microbiology: The Nitrogen and Sulfur Cycles*, J. A. Cole and S. J. Ferguson, Eds. (Cambridge Univ. Press, Cambridge, 1988), vol. 42, pp. 99–132.
- W. H. Campbell and J. R. Kinghorn, *Trends Biochem. Sci.* **15**, 315 (1990).
- J. M. Odom and R. Singleton Jr., Eds., *The Sulfate-Reducing Bacteria: Contemporary Perspectives*, (Springer-Verlag, New York, 1993).
- L. M. Siegel, M. J. Murphy, H. Kamin, *J. Biol. Chem.* **248**, 251 (1973); L. M. Siegel, P. S. Davis, H. Kamin, *ibid.* **249**, 1572 (1974).
- J. Ostrowski et al., *ibid.* **264**, 15726 (1989); J. Ostrowski et al., *ibid.*, p. 15796.
- L. M. Siegel and P. S. Davis, *ibid.* **249**, 1587 (1974).
- P. A. Janick, D. C. Rueger, R. J. Krueger, M. J. Barber, L. M. Siegel, *Biochemistry* **22**, 396 (1983).
- Y. Seki, N. Sogawa, M. Ishimoto, *J. Biochem.* **90**, 1487 (1981); Y. Seki and M. Ishimoto, *ibid.* **86**, 273 (1979); A. Soriano and J. A. Cowan, *J. Am. Chem. Soc.* **117**, 4724 (1995).
- L. M. Siegel et al., *J. Biol. Chem.* **257**, 6343 (1982).
- P. Janick and L. M. Siegel, *Biochemistry* **21**, 3538 (1982).
- W. A. Hendrickson, *Science* **254**, 51 (1991).
- SiRHP was purified as described (7) [see also J. Kaufman et al., *Biochemistry* **32**, 2853 (1993)]. Trypsin specific cleavage, confirmed by NH₂-terminal peptide sequencing, was promoted by incubating SiRHP (10 mg/ml) in 65 mM potassium phosphate (pH 7.7), 100 μM EDTA with trypsin (50 μg/ml) for 17 hours at 20°C; this reaction was halted by the addition of 50 μM phenylmethylsulfonyl fluoride (PMSF). Seed crystals (17) were grown by vapor diffusion from SiRHP (6 mg/ml), 65 mM potassium phosphate buffer, pH 7.7, 100 μM EDTA, 15 percent polyethylene glycol (PEG) MW 8000. Single, large (0.15 mm³ by 0.20 mm³ by 1.0 mm³) macrocrystals were produced by successive seeding into sitting drops of SiRHP (4 to 5 mg/ml) and decreasing PEG concentrations (15 to 11 percent). The growth rate was controlled by the addition of trypsin (100 ng/ml). The cleaved, crystallized hemoprotein (residues 74 to 570) retained native specific activity (within a factor of two) in a standard assay (24). The P2₁2₁2₁ crystal lattice, with one molecule per asymmetric unit and cell dimensions of 69.75 by 77.44 by 87.79 Å³, has V_m = 2.07 Å³/dalton and 40 percent solvent content.
- Heavy atom positions were found by means of Patterson techniques, confirmed by cross-Fourier maps calculated in XtalView (47) with phases derived from the EMTS derivative and native anomalous scattering, and then optimized by origin-removed Patterson refinement in HEAVY [T. C. Terwilliger and D. Eisenberg, *Acta Crystallogr.* **A39**, 813 (1983)]. Final MIRAS phasing and concomitant refinement against the lack of closure residuals was performed by PHASES [W. Furey and S. Swaminathan, *Am. Crystallogr. Mtg. Abstr.* (1990), p. 73]. Derivative data were scaled against native data collected on the same detector to limit systematic error. Xentronics data were processed with XENGEN [A. J. Howard et al., *J. Appl. Cryst.* **20**, 383 (1987)] and image plate data with MOSFLM [A. G. W. Leslie et al., *CCP4 Newslett.* **18**, 33 (1986)].
- D. E. McRee, D. C. Richardson, J. S. Richardson, L. M. Siegel, *J. Biol. Chem.* **261**, 10277 (1986).
- The MAD experiment (manuscript in preparation) utilized SSRL beam line 1-5, which was unfocused and equipped with a single Xuong-Hamlin area detector. Diffraction data were indexed with SSRL MWSYS software [written by E. A. Merritt, in W. A. Hendrickson et al., *Proc. Natl. Acad. Sci. U.S.A.* **86**, 2190 (1989)]; intensities were integrated with MADNESS [A. Messerschmidt and J. W. Pflugrath, *J. Appl. Cryst.* **20**, 306 (1987)]; absorption, Lorentz, and polarization corrections were applied with SSRL MWSYS; and initial batch scaling was performed by University of California, San Diego, multiwire software [A. J. Howard et al., *Methods Enzymol.* **114**, 452 (1985)] followed by local scaling between Bijvoet pairs and among wavelengths with the MADSYS program suite [W. Yang et al., *Science* **249**, 1398 (1990)]. Reflections with four or more observation restraints (51 percent of the data to 2.5 Å), were phased by MADLSQ [W. Hendrickson et al., *Proteins: Struct. Funct. Gen.* **4**, 77 (1988)]. An idealized cluster and siroheme iron were placed in a Bijvoet difference cross Fourier map calculated with amplitudes from MAD data ($\lambda = 1.7374$) and MIR phases alone, and then these positions were refined against the MAD data. Phase probability distributions based on lack-of-closure errors allowed incorporation of reflections with fewer than four phasing restraints, increasing the overall completeness to 69 percent. MAD phase distributions were cast into Hendrickson-Lattman coefficients with modified versions of MADABCD [A. P. Pähler et al., *Acta Crystallogr.* **A46**, 537 (1990)] and combined with similarly represented MIR phase information.
- Recombinant SeHP was expressed under control of the *CysJ/H* promoter (8) in the *E. coli* methionine auxotroph DL41 [W. A. Hendrickson et al., *EMBO J.* **9**, 1665 (1990)]. To augment overexpression from the *CysJ/H* promoter, we provided sulfate as the sole sulfur source and excluded complex vitamin supplements. As an isomorphous derivative, SeHP only slightly improved experimental phases. Of 11 possible selenomethione peaks, seven were above noise level in MAD-MIRAS phased difference Fourier maps when SeHP data were scaled against native data collected under the same conditions. Difference Fourier maps calculated with the refined model phases identified nine positions (two surface Met residues are disordered).
- After 63 percent of the unit cell scatterers were placed into MAD-MIRAS experimental maps with XFIT (47) (R factor 40.1 percent to 2.8 Å resolution), σ_A -weighted phase combination [R. J. Read, *Acta Crystallogr.* **A42**, 140 (1988)] substantially improved map quality and reduced phase errors. Eight additional cycles of refitting, refinement in X-PLOR [A. T. Brünger et al., *Science* **235**, 458 (1987)] and σ_A -weighted phase combination were needed to complete the protein model. The model was refined against native data 1 (Table 1) with an overall B factor of 20 Å² and then against native data 2 (Table 1) to 2.3 Å with individual B factors. As the resolution was increased to 2.0 Å, the model was refined and rebuilt three times to simulated annealed omit maps [A. Hodel et al., *Acta Crystallogr.* **A48**, 851 (1992)] that systematically excluded each one-tenth of the structure. The resolution was extended from 2.0 to 1.6 Å in four steps of 0.1 Å amid cycles of positional refinement, refitting to omit and 2F_o-F_c maps, and addition of waters. In the final stages of refinement stereochemical restraints for the cluster, bridging ligand, and siroheme iron were removed.
- Our crystallographic experiments have shown that the bound ligand exchanges with other anionic species (SO₃²⁻, NO₂⁻, CN⁻) in the absence of phosphate, and that subsequent re-introduction of phosphate reproduces the tetrahedral difference peak.
- The surface area loss on SNI_{RR} association (20 percent calculated with Areaimol and Diffarea as implemented in the CCP4 package [Collaborative Computational Project, Number 4, *Acta Crystallogr.* **D50**, 760 (1994)] and 18.7 percent calculated with MS [M. L. Connolly, *Science* **221**, 709 (1983)]) is comparable to that of other subunit interfaces [P. Argos, *Protein Eng.* **2**, 101 (1988)].
- Sequence citations: SynaSiR: G. Gisselmann, P. Klausmeier, J. D. Schwenn, *Biochim. Biophys. Acta* **1144**, 102 (1993); DvaSiR: J. Tan, L. R. Helms, R. P. Swenson, J. A. Cowan, *Biochemistry* **30**, 9900 (1991); ArfdSiR: C. Dahl, N. M. Kredich, R. Deutzmann, H. G. Truper, *J. Gen. Microbiol.* **139**, 1817 (1993); SynaNiR: I. Luque, E. Flores, A. Herrero, *Plant Mol. Biol.* **21**, 1201 (1993); SpiaNiR: E. Back, W. Burkhardt, M. Moyer, L. Privalle, S. Rothstein, *Mol. Gen. Genet.* **212**, 20 (1988); AnaNiR: I. L. Johnstone

- et al.*, *Gene* **98**, 181 (1990); EcdNIR: J. R. Kinghorn and E. I. Campbell, in *Molecular and Genetic Aspects of Nitrate Assimilation*, J. L. Wray and J. R. Kinghorn, Eds. (Oxford Science Publications, Oxford, 1989), pp. 385–403; AtNR: N. M. Crawford, M. Smith, D. Bellissimo, R. W. Davis, *Proc. Natl. Acad. Sci. U.S.A.* **85**, 5006 (1988); RatSO: R. M. Garrett and K. V. Rajagopalan, *J. Biol. Chem.* **269**, 272 (1994).
24. R. J. Krueger and L. M. Siegel, *Biochemistry* **21**, 2892 (1982).
 25. J. Lee, J. LeGall, H. D. Peck Jr., *J. Bacteriol.* **259**, 15373 (1973); I. Moura *et al.*, *Biochem. Biophys. Res. Commun.* **141**, 1032 (1986).
 26. J. F. Cline, P. A. Janick, L. M. Siegel, B. M. Hoffman, *Biochemistry* **25**, 7942 (1985).
 27. S. Han *et al.*, *ibid.* **28**, 5461 (1989); J. F. Madden, S. Han, L. M. Siegel, T. G. Spiro, *ibid.*, p. 5471.
 28. J. Kaufman, L. D. Spicer, L. M. Siegel, *ibid.* **32**, 2853 (1993).
 29. E. L. Bominaar, Z. Hu, E. Münck, J. Girerd, S. Borsch, *J. Am. Chem. Soc.* **117**, 6976 (1995).
 30. B. R. Crane and E. D. Getzoff, in preparation.
 31. C. K. Chang, L. K. Hanson, P. F. Richardson, R. Young, J. Fajer, *Proc. Natl. Acad. Sci. U.S.A.* **78**, 2652 (1981).
 32. W. R. Scheidt and C. A. Reed, *Chem. Rev.* **81**, 543 (1981).
 33. The sulfite complex was formed by soaking oxidized SiRHP crystals in 130 mM Hepes, 25 percent PEG 8K, 50 mM Na₂SO₃, at pH 7.9, anaerobically for 5 days. Diffraction data were collected on a Xenonics multiwire area detector mounted on a Rigaku Ru-200 rotating anode x-ray generator. The data set, reduced with XDS [W. J. Kabsch *et al.*, *J. Appl. Cryst.* **21**, 916 (1988)], was 93 percent complete to 2.2 Å with an R_{merge} on $I = 4.3$ percent. The crystals of sulfite and phosphate-bound SiRHP were isomorphous. Difference Fourier maps revealed substantial perturbations only at the active center. The structure was rebuilt with XFIT (47) and refined with X-PLOR [A. T. Brünger *et al.*, *Science* **235**, 458 (1987)] to a final R factor of 15.0 percent to 2.2 Å resolution, with 84 percent completeness after a 2σ cutoff on F .
 34. E. P. Day *et al.*, *Biochemistry* **27**, 2126 (1988).
 35. L. J. Young and L. M. Siegel, *ibid.*, p. 2790.
 36. C. C. Price and S. Oae, *Sulfur Bonding* (Ronald, New York, 1962).
 37. D. R. Lide, Ed., *Handbook of Chemistry and Physics* (CRC Press, Boca Raton, ed. 71, 1990).
 38. M. Schidlowski, J. M. Hayes, I. R. Kaplan, in *Earth's Earliest Biosphere, Its Origin and Evolution* (Princeton Univ. Press, Princeton, NJ, 1983), p. 149; J. R. Postgate, Ed., *The Sulfate-Reducing Bacteria*, (Cambridge Univ. Press, Cambridge, 1979); E. M. Cameron, *Nature* **296**, 145 (1982).
 39. M. Rutten, Ed., *The Origin of Life by Natural Causes* (Elsevier, Amsterdam, 1972).
 40. A. T. Brünger, *Acta Cryst.* **D49**, 24 (1993).
 41. M. Carson, *J. Appl. Cryst.* **24**, 958 (1991).
 42. Tubes were generated with the program MCS TUBES (Y. Chen and A. Olson) and rendered in the AVS environment [C. Upon *et al.*, *IEEE Comput. Graph. Appl.* **9**(4), 30 (1989)].
 43. Peptide sequencing indicated a secondary cleavage, at 1/2 to 1/10 the signal of the NH₂-terminal truncation, between residues 202 and 203.
 44. M. K. Gilson, A. Rashin, R. Fine, B. Honig, *J. Mol. Biol.* **183**, 503 (1985).
 45. R. J. Read, *Acta Cryst.* **A42**, 140 (1988).
 46. A. Hodel, S. H. Kim, A. T. Brünger, *ibid.* **A48**, 851 (1992).
 47. D. E. McRee, *J. Mol. Graphics* **10**, 44 (1992).
 48. We thank D. McRee for contributions to initial native and derivative diffraction data sets; J. Kaufman, J. Madden, P. Janick, for initial supplies of purified protein; J. Tainer for help with data collection; D. McRee and S. Mylvaganam for efforts at early map interpretation; H. Bellamy and P. Phizackerley for help with MAD data collection; W. Hendrickson for supplying the *E. coli* methionine auxotroph; J. Wu and N. Kredich for supplying the SiR holoenzyme clone; C. Nielsen, J. Pflugrath, E. Merritt, W. Weis, and T. Terwilliger for advice on data processing; C. Fisher for help with electrostatic calculations; M. Plaque for help with computer graphics; J. Tainer, H. Parge, C. Mol, G. Borgstahl, D. Hilvert, L. Noodleman, and W. Hendrickson for discussions; D. and J. Richardson for their support in transferring the SiRHP project to Scripps; and the Stanford Synchrotron Radiation Laboratory and the University of California at San Diego Research Resource for use of data collection facilities. Supported by NIH grants GM37684 (E.D.G.) and GM212226 (L.M.S.) and an NSERC 1967 fellowship (B.R.C.). Coordinates have been deposited in the Protein Data Bank.

5 April 1995; accepted 31 August 1995

AAAS–Newcomb Cleveland Prize

To Be Awarded for a Report, Research Article, or an Article Published in *Science*

The AAAS–Newcomb Cleveland Prize is awarded to the author of an outstanding paper published in *Science*. The value of the prize is \$5000; the winner also receives a bronze medal. The current competition period began with the 2 June 1995 issue and ends with the issue of 31 May 1996.

Reports, Research Articles, and Articles that include original research data, theories, or syntheses and are fundamental contributions to basic knowledge or technical achievements of far-reaching consequence are eligible for consideration for the prize. The paper must be a first-time publication of the author's own work. Reference to pertinent earlier work by the author may be included to give perspective.

Throughout the competition period, readers are

invited to nominate papers appearing in the Reports, Research Articles, or Articles sections. Nominations must be typed, and the following information provided: the title of the paper, issue in which it was published, author's name, and a brief statement of justification for nomination. Nominations should be submitted to the AAAS–Newcomb Cleveland Prize, AAAS, Room 924, 1333 H Street, NW, Washington, DC 20005, and **must be received on or before 30 June 1996**. Final selection will rest with a panel of distinguished scientists appointed by the editor-in-chief of *Science*.

The award will be presented at the 1997 AAAS annual meeting. In cases of multiple authorship, the prize will be divided equally between or among the authors.